Direct magneto-optical compression of an effusive atomic beam for application in a high-resolution focused ion beam

Direct Magneto-Optical Compression of an Effusive Atomic Beam for Application in a High-Resolution Focused Ion Beam

G. ten Haaf, T. C. H. de Raadt, G. P. Offermans, J. F. M. van Rens, P. H. A. Mutsaers, E. J. D. Vredenbregt,* and S. H. W. Wouters

Department of Applied Physics, Eindhoven University of Technology, P.O. Box 513, 5600 MB Eindhoven, The Netherlands

(Received 7 December 2016; revised manuscript received 2 March 2017; published 22 May 2017)

An atomic rubidium beam formed in a 70-mm-long two-dimensional magneto-optical trap (2D MOT), directly loaded from a collimated Knudsen source, is analyzed using laser-induced fluorescence. The longitudinal velocity distribution, the transverse temperature, and the flux of the atomic beam are reported. The equivalent transverse reduced brightness of an ion beam with properties similar to the atomic beam is calculated because the beam is developed to be photoionized and applied in a focused ion beam. In a single two-dimensional magneto-optical trapping step, an equivalent transverse reduced brightness of $(1.0^{+0.8}_{-0.4}) \times 10^6$ A/(m^2 sr eV) is achieved with a beam flux equivalent to $(0.6^{+0.3}_{-0.2})$ nA. The temperature of the beam is further reduced with an optical molasses after the 2D MOT. This optical molasses increases the equivalent brightness to $(6^{+5}_{-2}) \times 10^6$ A/(m^2 sr eV). For currents below 10 pA, for which disorder-induced heating can be suppressed, this number is also a good estimate of the ion-beam brightness that can be expected. Such an ion-beam brightness would be a 6× improvement over the liquid-metal ion source and could improve the resolution in focused ion-beam nanofabrication.

DOI: 10.1103/PhysRevApplied.7.054013

I. INTRODUCTION

Laser cooling and compression is used to intensify atomic beams for use in a variety of physics experiments, such as the loading of magneto-optical traps (MOTs), beam collision studies [1] and atom interferometry [2]. An emerging field of application is the ionization of such cold atomic beams to create high-brightness ion beams which can be applied in focused ion beams (FIBs) [3]. FIBs are tabletop instruments in which nanoscale devices can be inspected, by gathering secondary electrons or ions, and fabricated, by etching and ion-beam-induced deposition [4–6]. For these applications, the most important figures of merit are the transverse reduced brightness and the energy spread of the ion beam as they determine the FIBs resolution together with parameters of the electrostatic lens column. The ion source currently used in most of the commercial FIBs for high-resolution nanofabrication purposes is the liquid-metal ion source (LMIS). This source offers a transverse reduced brightness of 10^6 A/(m^2 sr eV) [6,7] and a full-width-at-half-maximum energy spread of 4.5 eV [6,8]. With this beam quality, a LMIS-based FIB has a resolution of roughly 5 nm when operated at 30 kV with a beam current of 1 pA [6,9].

Several research groups worldwide have been working on alternative ion sources based on the field ionization or photoionization of cold atoms. The first realizations [10,11] consist of a magneto-optical trap from which the ions are created and extracted. The ion current, and therefore also the reduced brightness, from these sources is limited by the slow refilling rate of the ionization volume inside the MOT. Several proposals [12–15] have been made to overcome this problem by creating a cold atomic beam instead of a MOT, which is subsequently ionized.

There are several routes in creating a cold atomic beam. In a so-called 2D$^+$ MOT [16], background vapor atoms are captured in a 2D MOT in which they are also laser cooled in the third dimension. Through a dark spot in one of those third-dimension laser beams, slowly traveling atoms can escape. This strategy has been proven to produce a flux of 2×10^{10} ^{85}Rb atoms/s [17]. By replacing the third-dimension laser beams with a pair of hollow cooling beams and an additional pushing beam in the center, the flux can be further optimized. This optimization has recently been investigated, resulting in a flux of 4×10^{10} Cs atoms/s [18]. Without the additional cooling in the third dimension—that is, with a pure 2D vapor-cell MOT—a flux of 6×10^{10} of faster-traveling ^{87}Rb atoms/s is produced [19]. A so-called pyramidal MOT [20] has also been used in the past to create a lower flux of 4×10^9 Cs atoms/s [21], but with the advantage of only a single laser-cooling beam being used. Instead of capturing the atoms from the background vapor, one can produce similarly valued atomic fluxes by loading a 2D MOT from the transverse direction with an effusive source [22,23]. However, in all cold-atomic-beam experiments mentioned so far, the goal was to produce a large flux of, preferably, slowly traveling atoms.

*e.j.d.vredenbregt@tue.nl

In the research presented here, the goal is different. Here, the figure of merit is the brightness of the atomic beam instead of the flux. Furthermore, for the intended application of transforming the atomic beam in a high-brightness ion beam, the longitudinal velocity of the atoms is less important, which makes longitudinal loading of a 2D MOT with an effusive source an option. Longitudinal loading of a 2D MOT has already been done in the past; however, in these experiments, a Zeeman slower is usually used in order to slow down the atoms before entering the 2D MOT [24,25], which drastically increases the size of the apparatus. Furthermore, Tsao *et al.* investigated the relative performance of a 2D MOT directly loaded in the longitudinal direction with a thermal beam of sodium atoms for different longitudinal velocity groups [26].

Here, experimental results are presented of the atomic-beam formation in the atomic-beam laser-cooled ion source (ABLIS), in which a 2D MOT is directly loaded from a collimated Knudsen source [27] and used to create a high-brightness ^{85}Rb atom beam. Extensive simulations of this source, which assume that all atoms in the beam can be transformed into ions—and that includes the interaction of the ions after ionization—predict that when combined with a conventional electrostatic focusing column, 1 pA of 30-keV rubidium ions can be focused to a 1-nm spot [15,28]. This strategy provides an alternative to the FIB source developed by Knuffman *et al.* [13], in which a high-brightness cesium beam is made by compressing the beam formed in a $2D^+$ MOT further in a magneto-optical compressor. Recently, other researchers realized an ion microscope which was based on the field ionization of a transversely cooled beam of cesium atoms also originating from a thermal source [14,29]. Here, no 2D trapping or compression is applied, and the transverse reduced brightness of the ion beam is estimated at 2.8×10^5 A/(m^2 sr eV).

In this paper, the quality of the atomic beam after the 2D MOT in the ABLIS setup is analyzed by means of laser-induced fluorescence (LIF). The improvement of the beam quality with an additional optical molasses step is also explored. The longitudinal velocity distribution, the beam flux, and the transverse temperature are measured. Also, the equivalent transverse reduced brightness is determined, which is defined as the brightness of an ion beam with a similar temperature and flux density as the atomic beam. Section II describes the experimental setup in which the experiments are done and the methods used, after which the experimental results are presented in Sec. III. Section IV presents the conclusions.

II. METHODS

Figure 1 shows a schematic picture of the experimental setup. Note that in the actual experiment, the beam travels in the vertical direction since this will also be the orientation of the source when mounted on a FIB system. As shown, an atomic rubidium beam from a collimated Knudsen source [27] with temperature T_s effuses into a

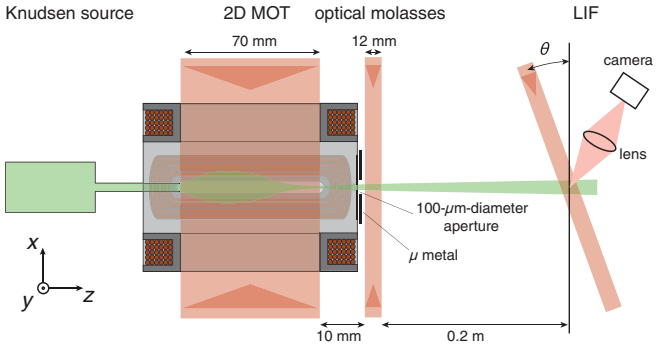

FIG. 1. Overview of the experimental setup (not drawn to scale). An atomic rubidium beam effusing from a collimated Knudsen source is cooled and compressed by means of two sets of σ^+/σ^- polarized laser beams and a compact in-vacuum quadrupole electromagnet with an iron core, which together form a 2D MOT. A μ-metal plate shields the region after the electromagnet from magnetic fields and an aperture selects the central part of the beam. An optical molasses can be created with two sets of laser beams with a lin-perp-lin polarization configuration to further reduce the transverse temperature of the beam. The atomic beam is allowed to drift for 0.2 m, where its profile is imaged onto a camera using laser-induced fluorescence (LIF). The direction of travel of the probe beam can be altered to make an angle θ with the transverse direction of the atomic beam in order to determine the longitudinal velocity distribution. Note that, in the actual experiment, the atoms travel in the vertical direction.

2D MOT [30]. After the 2D MOT, the atoms can be cooled to a sub-Doppler temperature with a second set of counter-propagating laser beams, forming an optical molasses. After a 0.2-m drift, a probe laser beam is used to visualize the atomic beam by means of laser-induced fluorescence (LIF), which is imaged onto a camera. Although laser absorption measurements allow a very accurate determination of the beam density [31], the choice is made to use LIF, for this is an established technique for beam characterization as well [16,17,19,22,24,25]. From the divergence of the atomic beam, the temperature is calculated, while the intensity of the LIF signal allows the determination of the flux of the beam. Both of these calculations require knowledge about the longitudinal velocity distribution of the atoms in the beam. By placing the probe under an angle with respect to the atomic beam and scanning its frequency, this distribution is determined.

The remainder of this section is divided into three parts. First, the details of the experimental setup are described. Then the methods to determine the flux, the transverse temperature, and the equivalent transverse reduced brightness are introduced and, finally, the method to measure the longitudinal velocity distribution is explained.

A. Experimental setup

The compact 2D MOT is created with an in-vacuum electromagnet with a pure iron core, capable of creating a

two-dimensional quadrupole field with a magnetic field gradient ∇B of 3.8 T/m. Four identical laser-beam expansion modules (not shown in the figure) generate the required laser fields with a σ^+/σ^- polarization scheme and a $1/e^2$ diameter of 12 mm in the transverse direction (x or y) and 120 mm in the longitudinal (z) direction. The peak intensity of each of the four 2D MOT beams is 98 W/m^2 (a saturation intensity $I_{\mathrm{sat}} = 16.7$ W/m^2 [32] gives a saturation parameter of $s = 5.9$). The yoke of the magnet has 70-mm-long slots milled into it to allow the laser beams to reach the center.

Downstream of the 2D MOT laser beams, there is a 10-mm-long drift space in which the atoms do not see laser light and in which the magnetic field (gradient) decreases. At the end of the yoke, a μ-metal plate is placed to shield the region behind the yoke from magnetic fields to allow for additional sub-Doppler cooling. The residual magnetic field gradient after this μ-metal plate is measured to be 0.05 T/m. Finite-element calculations of the magnetic field in the quadrupole magnet show that the distortion of the field inside the quadrupole is less than 3%. An aperture with a 100-μm diameter is also placed after the 2D MOT for beam selection. An imbalance is made in the currents through the four coils of the quadrupole magnet to steer the atomic beam through the selection aperture. An optical molasses is created directly after the selection aperture with two pairs of counterpropagating laser beams, with a $1/e^2$ diameter of 12 mm and a peak intensity of 1.5×10^2 W/m^2 ($s = 4.8$ for $I_{\mathrm{sat}} = 31.8$ W/m^2 [32]). The polarizations of these laser beams are chosen such that, in both directions, a lin-perp-lin configuration is achieved.

Laser-induced fluorescence is used to determine the important atomic-beam properties. At a distance of $\Delta z = 0.20$ m from the beam selection aperture, a probe laser beam propagating over the line $x = y$ is crossed with the atomic beam. This probe beam has a $1/e^2$ diameter of 11.5 mm, is linearly polarized in the z direction and has a peak intensity of 1.9 W/m^2 ($s = 0.06$ for $I_{\mathrm{sat}} =$ 31.8 W/m^2 [32]) in the longitudinal velocity distribution measurements and 96 W/m^2 ($s = 3.1$ for $I_{\mathrm{sat}} =$ 31.8 W/m^2 [32]) in all other measurements shown. The fluorescent light emitted by the atoms is imaged onto two cameras: one looking at the beam in the x direction and one in the y direction. This method allows the determination of the temperature of the atomic beam in both transverse directions. Each measurement series is started with a camera image, with the probe laser far detuned. This image is subtracted from all other images in the measurement to correct for background scattering.

The laser light for the 2D MOT and optical molasses is generated using a Coherent 899-21 Ti:sapphire ring laser. This laser is frequency stabilized at the crossover resonance between the $5\,^2S_{1/2}F = 3$ to $5\,^2P_{3/2}F' = 2$, 4 transitions of ^{85}Rb in the frequency-modulation spectrum [33]. An acousto-optical modulator in a double-pass configuration is used to shift the laser frequency to the desired detuning δ from the $5\,^2S_{1/2}F = 3$ to $5\,^2P_{3/2}F' = 4$ cooling transition. A resonant electro-optical modulator is used to generate sidebands at 2918 MHz from the laser-cooling frequency, of which the positive sideband is used for repumping. Note that the repumping detuning is therefore coupled to the cooling detuning. Since the frequency difference between the cooling and repumping transition is 2915 MHz, this means that the repumping detuning is approximately zero when the cooling detuning is set to half a linewidth from the cooling transition. The cooling and repumping light is coupled into a polarization maintaining fiber that splits in four and is connected to the optical modules that shape the laser beams for the 2D MOT and the additional optical molasses. The light in the probe laser beam is generated using a Toptica DL100-XXL diode laser. This laser is frequency stabilized by means of a frequency offset lock that keeps the frequency difference within 100 Hz of the desired difference with respect to the Ti:sapphire laser frequency. Varying the set point of this system allows us to set the probe laser detuning δ_p within a range of -90 to 100 MHz.

B. Beam flux, temperature, and brightness

In this section, the equations are presented with which the temperature, the flux, and the equivalent brightness of the atom beam are extracted from the LIF measurements. A simple model is set up to describe the transverse density profile of the beam after the drift from the selection aperture to the probe laser beam. This profile depends on the velocity distribution of the atoms, so it can be used to determine the transverse temperature of the beam. Also, the equations for determining the atomic flux and density of the beam from the intensity of the LIF signal are given. Finally, the relations between flux, temperature, and equivalent brightness are presented.

After an atom drifts over a length Δz, its transverse position x_2 is given by $x_2 = x_1 + \Delta z v_x/v_z$, in which x_1 is the initial transverse position, v_x is the transverse velocity, and v_z is the longitudinal velocity of the atom. Assuming that x_1, v_x, and v_z are uncorrelated and v_x is distributed according a normal distribution with root-mean-square (rms) width σ_{v_x}, the mean-square size of the distribution in x_2 is given by

$$\langle x_2^2 \rangle = \langle x_1^2 \rangle + (\Delta z)^2 \sigma_{v_x}^2 \langle 1/v_z^2 \rangle, \tag{1}$$

and the transverse temperature T_x of the beam can be written as

$$T_x = \frac{m\sigma_{v_x}^2}{k_B} = \frac{m}{k_B}\left(\frac{\tilde{v}_z}{\Delta z}\right)^2 (\langle x_2^2 \rangle - \langle x_1^2 \rangle), \tag{2}$$

in which m is the mass of the atom (taken from Ref. [32]), k_B is the Boltzmann constant, and $\tilde{v}_z = 1/\sqrt{\langle 1/v_z^2 \rangle}$.

Finding the transverse temperature now relies on measuring $\langle x_2^2 \rangle$. Under the assumption that all of the atoms are resonant with the probe laser, the LIF profile will have the same width as the distribution of x_2. This assumption requires that the Doppler shift of the atoms due to their transverse velocity is smaller than the linewidth Γ [32] of the transition, i.e., $2\pi\sigma_{v_x}/\lambda < \Gamma$, in which λ is the wavelength of the transition. This assumption is valid for transverse beam temperatures lower than 0.2 K, which is easily achieved in the experiment. The initial position x_1 is assumed to be uniformly distributed over the circular selection aperture. Such a distribution gives $\langle x_1^2 \rangle = R/2$, in which R is the radius of the selection aperture. As will be shown later, this value is significantly smaller than the spread due to the divergence of the beam, which results in the distribution in x_2 resembling a normal distribution very well. Therefore, $\langle x_2^2 \rangle$ is found by fitting such a distribution to the LIF profile.

The scattering rate of LIF photons R_{ph} can be found from the intensity C of the LIF signal. C is acquired by calculating the area under the normal distribution fitted through the LIF profile and is expressed in camera counts. Using its value, R_{ph} can be calculated with

$$R_{\mathrm{ph}} = \frac{C}{G t_c T_{\mathrm{geom}} T_w T_f}, \tag{3}$$

in which G is the number of counts measured by the camera per incident photon, t_c is the shutter time of the camera, $T_{\mathrm{geom}} = \pi r_1^2/(4\pi o^2)$ is the part of the isotropic emission sphere that the imaging lens with radius r_1 at a distance o from the atomic beam covers, and T_w and T_f are the transmission of the vacuum window and a filter to reduce background light. The beam flux Φ is calculated from the scattering rate using

$$\Phi = \frac{R_{\mathrm{ph}}}{\langle t_{\mathrm{tr}} \rangle \rho_{ee}(0)\Gamma}, \tag{4}$$

in which $\langle t_{\mathrm{tr}} \rangle$ is the average transfer time through the imaging volume and $\rho_{ee}(\delta_p)$ is the excited-state population as a function of the probe laser detuning δ_p, which is given by [34]

$$\rho_{ee}(\delta_p) = \frac{\frac{s_0}{2}}{1 + s_0 + \left(\frac{2\delta_p}{\Gamma}\right)^2}, \tag{5}$$

where $s_0 = I/I_{\mathrm{sat}}$ is the saturation parameter, in which I is the laser-beam intensity and I_{sat} is the saturation intensity [32]. The average transfer time through the imaging volume is given by $\langle t_{\mathrm{tr}} \rangle = l/\overline{v_z}$, in which l is the longitudinal width of the imaged volume and $\overline{v_z} = 1/\langle 1/v_z \rangle$. Note that, by writing down Eq. (4), the assumption is made that every photon that is emitted by an atom in the direction of the imaging lens also reaches the camera, i.e., reabsorption does not play a role. In Sec. III E, we show that this is a valid approximation.

If all atoms are ionized, the beam current will be $I = e\Phi$ in which e is the elementary charge. With the intended application of the beam in a FIB system in mind, the measured flux is reported in amperes as an equivalent ion current throughout this paper.

Instead of the beam flux, the average beam density n at the selection aperture, can be calculated using

$$n = \frac{R_{\mathrm{ph}}}{\pi R^2 l \rho_{ee}(0)\Gamma}. \tag{6}$$

Note that this quantity can be determined without knowing the longitudinal velocity of the atoms.

Assuming that there are no correlations between x and v_x and y and v_y at the position of the selection aperture, that the atoms are uniformly distributed over this circular selection aperture, and that v_x and v_y are distributed according to a normal distribution, the transverse reduced brightness of an ion beam with equal properties to that of the atomic beam can be calculated with [35]

$$B_r = \frac{e\Phi}{\pi^2 R^2 k_B \sqrt{T_x T_y}}. \tag{7}$$

Note that, if there are correlations between transverse position and velocity at the selection aperture, the equivalent brightness will be higher than this calculated value. Furthermore, if the atoms are not uniformly distributed over the aperture, the brightness will be higher as well. This means that the calculated value is a lower limit of the actual peak equivalent brightness. Note that, for presenting the number from Eq. (7) in units of $\mathrm{A}/(\mathrm{m^2\,sr\,eV})$, multiplication by a second factor e is required.

Transforming the atomic beam into an ion beam without giving in on the order of magnitude of transverse reduced brightness is a challenging but not impossible task. First of all, a high ionization efficiency is desired. One can estimate [15] that, in a two-step photoionization process in which the excitation light is resonant and the ionization light is above threshold, an ionization degree of 80% can be achieved within a length of 3 μm with an ionization laser-beam intensity of 2×10^{10} $\mathrm{W/m^2}$. With a laser producing 500 mW of light at the ionization wavelength of 480 nm, this intensity can be realized by focusing the laser beam to a $1/e^2$ beam diameter of 8 μm. When a buildup cavity is used, a similar intensity can also be achieved over a larger area. Alternatively, one can use Rydberg excitation and field ionize the atoms [14,29]. Another point of importance is that the ions will strongly interact after ionization, which can lead to a degradation of the brightness due to disorder-induced heating. However, in previous work [28], simulations were presented which

show that, for currents below 10 pA, these interactions can be suppressed by accelerating the ions in a large but realistic electric field. With both of these aspects considered, the equivalent transverse reduced brightness presented in this manuscript also gives a realistic estimate of the order of magnitude of the transverse reduced brightness of a 10-pA ion beam that can be made from it. The creation of higher currents is also possible, but interactions will then limit the transverse reduced brightness.

An estimate of systematic uncertainties in the experiment is made (see the Appendix). Because of the many factors involved in the scattering, collection, and conversion of LIF photons, error margins for the temperature ($^{+62}_{-37}$ %), the flux ($^{+51}_{-32}$ %), the density ($^{+48}_{-31}$ %), and the brightness ($^{+80}_{-38}$ %) are quite substantial.

C. Longitudinal velocity distribution

In the calculation of all important beam parameters, the value of either $\overline{v_z}$ or $\tilde{v_z}^2$ plays an important role. As can be seen in Eqs. (2) and (4), the measured temperature scales with $\tilde{v_z}^2$ and the measured flux with $\overline{v_z}$. As shown by Eq. (7), this means that the measured brightness scales with $\overline{v_z}/\tilde{v_z}^2$. One could assume that the longitudinal velocity of the atoms in the beam is distributed according to a Maxwell-Boltzmann distribution with the temperature of the source T_s. However, because of the finite length of the 2D MOT, it is to be expected that atoms with a higher longitudinal velocity are laser cooled less effectively and thus have a lower probability of being transmitted through the selection aperture. Therefore, the values of $\overline{v_z}$ and $\tilde{v_z}^2$ are acquired experimentally to prevent any errors in the determination of the beam quality due to a wrongly estimated longitudinal velocity.

The longitudinal velocity distribution $p(v_z)$ is determined by looking at the intensity $F(\delta_p)$ of the fluorescence signal as a function of the detuning of the probe laser beam, which is now oriented so that it makes an angle $\theta = (14.8 \pm 0.5)°$ with the atomic beam; see Fig. 1. In this way, the longitudinal velocity of the atoms will cause a Doppler shift in the frequency of the laser, so that the effective detuning becomes $\delta_p - (2\pi/\lambda)v_z \sin\theta$. Therefore, $F(\delta_p)$ becomes dependent on the longitudinal velocity of the atoms. This dependence can be expressed in a proportionality given by

$$F(\delta_p) \propto \int_0^\infty \frac{p(v_z)}{v_z} \rho_{ee}[\delta_p - (2\pi/\lambda)v_z \sin\theta] dv_z, \quad (8)$$

which explicitly includes all dependence on the longitudinal velocity of the atoms. It shows that $F(\delta_p)$ is a convolution of the line shape of the transition with $p(v_z)/v_z$, in which the extra factor of $1/v_z$ compensates for the fact that the transfer time through the imaged volume is smaller for faster-traveling atoms, which therefore contribute less to the fluorescence than slower-traveling atoms.

To find $p(v_z)$, the measured data need to be deconvoluted from the linewidth of the transition. Since numerical deconvolution is difficult, the data are fitted with a test function that represents $p(v_z)/v_z$, which is convoluted with $\rho_{ee}(\delta_p)$. For the test function, a sixth-order polynomial $P_6(v_z)$ is chosen, multiplied by a Gaussian distribution $e^{-(v_z^2/a^2)}$, in which a is a fitting parameter and $P_6(v_z)$ contains the other seven fitting parameters. This means that, after fitting the data, $p(v_z)$ is calculated with

$$p(v_z) = C_n v_z P_6(v_z) e^{-(v_z^2/a^2)}, \quad (9)$$

in which C_n is a normalization constant. The resulting distribution is finally used to calculate the required moments $\bar{v_z}$ and $\tilde{v_z}^2$.

Note that the test function in this fitting routine is not based on any physical argument. Since the goal is not to find an analytical expression for the distribution but to deconvolute the measured data from the linewidth of the transition, a test function with a large number of fitting parameters is chosen that gives a precise fit to the measured data. The chosen test function does make sure that the distribution goes to zero in the limits of v_z to zero and to infinity.

III. RESULTS

In this section, the measurements of the atomic-beam parameters are discussed. As the values of $\overline{v_z}$ and $\tilde{v_z}^2$ are needed in order to calculate the equivalent brightness of the beam, the longitudinal velocity distribution measurement is discussed first.

A. Longitudinal velocity distribution

Figure 2 shows an example of a longitudinal velocity distribution measurement. The measured data are fitted as described in Sec. II C. As can be seen, the large number of fitting parameters enables a good fit with the data. The normalized longitudinal velocity distribution that is obtained from this measurement is plotted in Fig. 3. The distribution yields an average velocity of (83 ± 3) m/s. This value is much smaller than the average velocity of the thermal atoms in the Knudsen source, which is 321 m/s. The uncertainty in the average is the uncertainty arising from the deconvoluting fitting procedure. It is estimated by looking at the spread in the results when the polynomial in the fitting function contains more or fewer orders. Apart from this spread, there is also a systematic uncertainty on the value of 2 m/s due to the uncertainties in θ_p and the absolute value of δ_p.

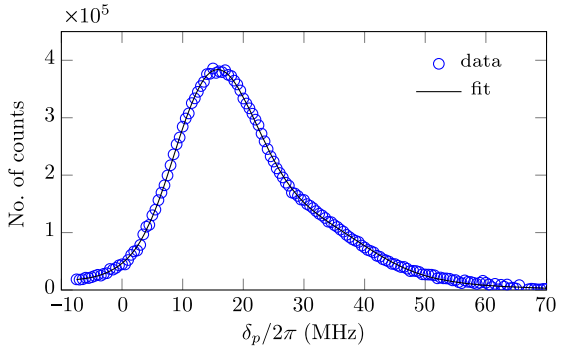

FIG. 2. Laser-induced fluorescence signal as a function of the laser detuning. The laser makes an angle $\theta = 14.8°$ with the transverse direction of the atomic beam. To extract the longitudinal velocity distribution, the data are fitted with a sixth-order polynomial that is multiplied by a Gaussian and convoluted with Eq. (5). This measurement is performed with $\nabla B = 0.94$ T/m, $\delta = -1.1\Gamma$, and $T_s = 433$ K.

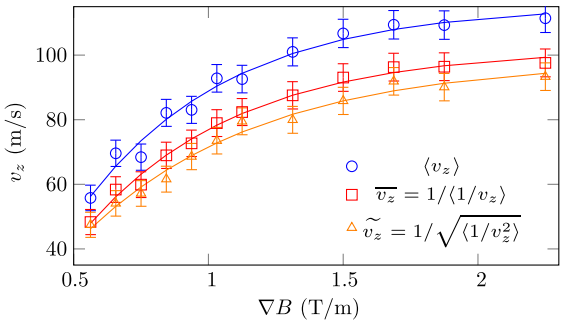

FIG. 4. Important moments of the longitudinal velocity distribution as a function of the magnetic field gradient. The error bars show the uncertainty originating from the deconvoluting fitting procedure, which is estimated at 3 m/s. The fit is performed with an asymptotic exponential growth function. This fit function has no physical meaning but serves as a guide for the eye in this figure. It is employed in further analysis in which the moments are used to calculate the flux, the temperature, and the equivalent brightness of the beam. The data are measured with $\delta = -1.1\Gamma$ and $T_s = 433$ K.

As the measured longitudinal velocity distribution in Fig. 3 results from a deconvolution, it is important to mention that features within a velocity span of approximately $\Gamma/k \sin\theta = 18$ m/s are washed out and not properly represented. Nevertheless, there are some distinct features that are apparent in the distribution at a larger scale. For example, after the maximum of the distribution, there appears to be a second bump. This bump is found to be more pronounced at larger magnetic field gradients. At the highest gradients, this second maximum even becomes the global maximum in the distribution. The reason for this bimodal shape of the distribution is not known. An explanation for the shift to higher average velocities at larger gradients is given below.

Another characteristic of the distribution is that there are no atoms with a velocity below approximately 20 m/s. Part of the explanation for this phenomenon lies in the fact that the atoms travel through a region of 10 mm with no laser cooling and compression before being selected by the selection aperture. The slower the atoms travel longitudinally, the larger the divergence of these atoms is in this region, which lowers the probability of being transmitted through the aperture. Furthermore, after the selection aperture, slower-traveling atoms also have a larger divergence, which means that they are more spread out at the position where they are imaged. Therefore, their fluorescence is less intense and, at low-enough velocities, becomes smaller than the noise level in the images.

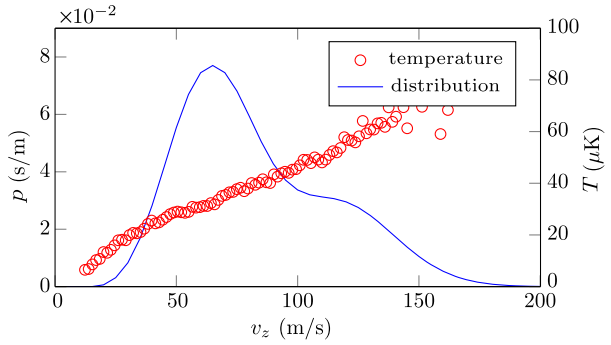

FIG. 3. Longitudinal velocity distribution and a plot of the transverse temperature against the longitudinal velocity. The longitudinal velocity distribution is found from the data plotted in Fig. 2. The measurement is performed with $\theta = 14.8°$, $\nabla B = 0.94$ T/m, $\delta = -1.1\Gamma$, and $T_s = 433$ K.

Similar measurements are performed at different magnetic field gradients. Figure 4 shows the average velocity and the two moments required in the calculation of the reduced brightness as a function of the magnetic field gradient. Below 0.5 T/m, the fluorescence signal is not high enough to perform reliable measurements. Between 0.5 and 1.5 T/m, the averages increase, which can be explained by the fact that, by increasing the magnetic field gradient, the spring constant of the 2D MOT becomes larger. This larger spring constant enables the trapping of faster-traveling atoms that do not have enough time to be pushed to the axis at lower gradients. Above a gradient of 1.5 T/m, the averages do not change much. The values of $\bar{v}_z$ and $\tilde{v}_z{}^2$ are used to calculate the flux, the temperature, and the equivalent reduced brightness in the next section. Instead of interpolating between measured values, the data shown in Fig. 4 are fitted with an asymptotic exponential growth function in order to get values for $\bar{v}_z$ and $\tilde{v}_z{}^2$ at magnetic field gradients between 0.5 and 2.5 T/m.

In the derivation of Eq. (2), the assumption is made that no correlation exists between v_x and v_z. In this measurement of the longitudinal velocity distribution, it is possible to check to what extent this approximation is valid. This validation is accomplished by looking at the divergence of

different velocity groups in the atomic beam, i.e., by also determining the rms size of the beam at each detuning and using Eq. (2) to determine the temperature at which $\delta_p/k \sin\theta$ is now used for the longitudinal velocity instead of $\tilde{v}_z$. The results are shown in Fig. 3. As can be seen, slower-traveling atoms are cooled to a lower temperature than faster-traveling atoms, which is to be expected due to the longer time they spend in the optical molasses. The approximation made in writing Eq. (1) is $\langle (v_x^2)/(v_z^2)\rangle \approx \langle v_x^2\rangle\langle 1/(v_z^2)\rangle$. However, Fig. 4 shows that the average of v_x^2 is a linear function of v_z. Substituting a linear relation value into the approximation above leads to $\langle 1/(v_z)\rangle \approx \langle v_z\rangle\langle 1/(v_z^2)\rangle$. Using the measured velocity distributions, the fractions of the left- and right-hand sides of this approximation can be calculated to be within 0.74–0.8 over the whole range of measured magnetic field gradients. This means that the temperature calculated with Eq. (2) yields a 25%–35% overestimation of the actual temperature.

B. Beam profiles

Figure 5 shows several transverse fluorescence profiles of the atomic beam. In the measurements shown in the top panel, labeled as "2D MOT only," the optical-molasses laser beams are turned off, while, in the measurements shown in the bottom panel, labeled as "with opt. mol.," they are enabled. As is apparent from the figures, increasing the magnetic field gradient increases the intensity of the LIF signal. Furthermore, without the optical molasses, it also leads to a broader profile. With the optical molasses enabled, this does not happen, indicating that the divergence of the beam is indeed reduced. Careful analysis of the profiles teaches us that, without optical molasses, the center of the profiles do not overlap for different magnetic field gradients. The profiles are also slightly asymmetric in this case. Since this does not happen with the optical molasses enabled, it is attributed to asymmetries in the 2D MOT, e.g., the imbalance in the currents through the coils of the magnetic quadrupole that enables the steering of the beam through the selection aperture. By creating this imbalance, the magnetic axis (where $B = 0$) overlaps with the selection aperture, but the pointing of the atomic beam can be altered as well. With the optical molasses enabled, the pointing of the resulting atomic beam is determined only by the orientation of the optical-molasses laser beams and thus is independent of the magnetic field gradient. The figures also show the Gaussian fits through the profiles, which are used for further analysis. In the measurements with the optical molasses enabled, the fits overlap nicely with the data. Because of the asymmetries in the profiles, the overlap is less satisfactory without the optical molasses, but it is still good enough to analyze the beam properties.

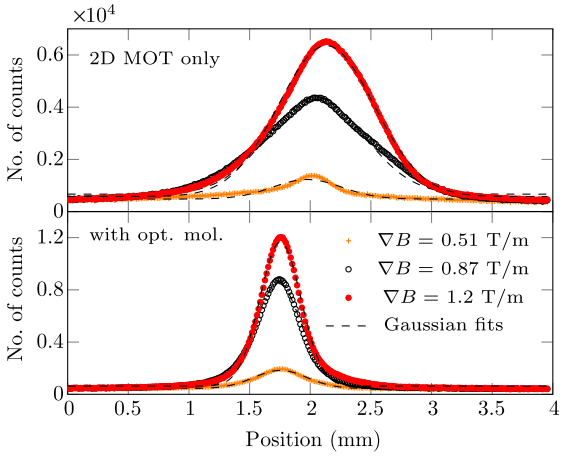

FIG. 5. Transverse beam profiles (the dots, circles, and plus signs) after the 2D MOT and a drift of 0.20 m in cases (bottom panel) with and (top panel) without optical molasses. The profiles are shown for different magnetic field gradients. The figure also shows the Gaussian fits (the dashed lines) which are used for analysis of the temperature, the flux, and the equivalent brightness of the beam. The data are measured with $\delta = -1.1\Gamma$ and $T_s = 413$ K.

C. Effect of cooling-laser detuning

An important parameter in the laser-cooling and compression process is the detuning of the cooling laser. A large negative detuning results in a large capture velocity but a small damping rate of the velocity of the atoms, whereas a small negative detuning results in a small capture velocity but a high damping rate [34]. To find the optimum in this trade-off, the detuning is varied and the LIF intensity and profile are monitored. Figure 6 shows the results of this experiment in which the optical molasses is disabled. The absolute frequency of the cooling laser is not determined accurately, so the detuning axis is shifted in such a way that no counts are achieved at $\delta = 0$. The results confirm the trade-off between capture velocity and damping rate. The LIF signal increases from $\delta = 0$ to $\delta = -1.1\Gamma$, indicating

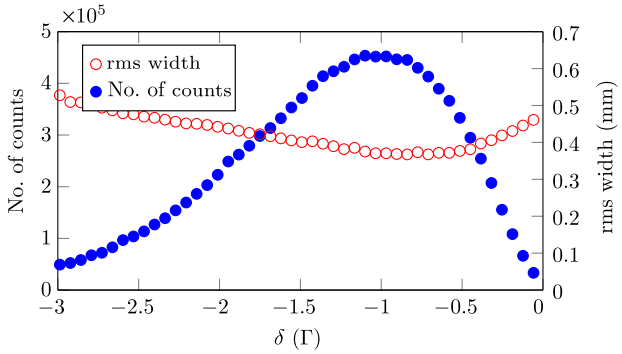

FIG. 6. Total LIF intensity and rms beamwidth after 0.2 m drift as a function of the detuning of the cooling laser. The data are measured with $\nabla B = 1.2$ T/m and $T_s = 413$ K.

the density as the selection aperture increases. Decreasing the detuning further from $\delta = -1.1\Gamma$ reduces the LIF signal again. The rms width also shows the trade-off: lowering the detuning leads to a decrease, a minimum is achieved at $\delta = -0.8\Gamma$, and lowering the detuning even further increases the rms width again. For a two-level atom in an infinitely long laser cooler (no trapping) with near-zero saturation intensity, the lowest temperature is reached at $\delta = -\Gamma/2$ [36]. Optimum flux and temperature in the experiment are reached at a different detuning. The finite length of the 2D MOT, the trapping, the high saturation parameter, and the sub-Doppler effects arising from the multilevel structure of the atom are possible explanations for this difference. All of the other measurements shown are therefore carried out at $\delta = -1.1\Gamma$.

D. Effect of the magnetic field gradient

Another important parameter determining the properties of the atomic beam is the magnetic field gradient. Similar to the detuning, a small magnetic field gradient leads to a large capture range but a small spring constant [34], pulling the atoms towards the magnetic axis. On the other hand, a high magnetic field gradient leads to a small capture range but a high spring constant. Furthermore, the presence of a magnetic field can inhibit sub-Doppler cooling mechanisms that occur due to the σ^+/σ^- laser-beam configuration. Figure 7 shows the flux, the transverse temperature, and the equivalent brightness as a function of the magnetic field gradient for the experiments with and without additional optical molasses. The longitudinal velocity distribution is only measured for magnetic field gradients in the range 0.5–2.5 T/m. Since $\bar{v}_z$ and $\tilde{v}_z$ are needed in the calculation of all of the parameters shown, they are not determined below 0.5 T/m. Because of the trend shown in Fig. 4, $\bar{v}_z$ and $\tilde{v}_z$ are assumed to be constant and equal to their values at 2.5 T/m for values above this magnetic gradient.

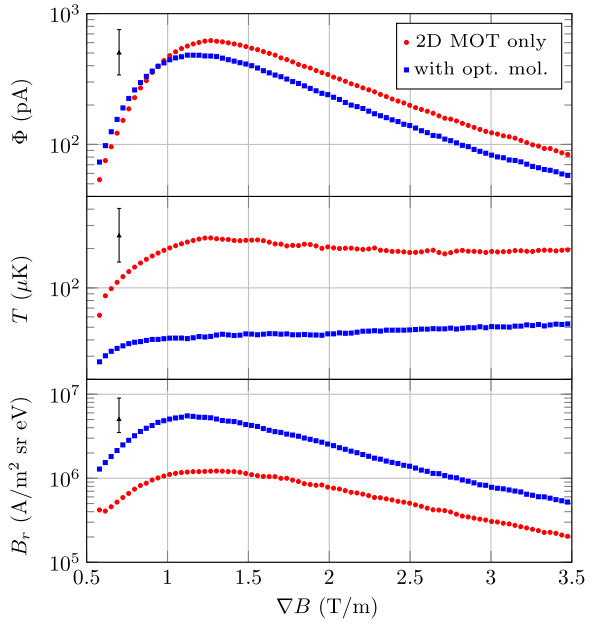

FIG. 7. Flux, transverse temperature, and equivalent brightness of the atomic beam as a function of different magnetic field gradients. The results with (squares) and without (circles) additional optical molasses are shown. The relative uncertainty margin due to systematic errors is indicated by black bars in the upper-left corner of each graph. In the middle graph, the temperatures shown are the average of the temperatures in the two transverse directions. The data are measured with $T_s = 413$ K and $\delta = -1.1\Gamma$.

In the top graph, the beam flux through the selection aperture is shown in amperes, resembling the maximum ion current that can be made from the atomic beam. As expected, the flux increases when the magnetic field gradient is raised and decreases again after reaching an optimum. The highest flux, equivalent to $(0.5^{+0.3}_{-0.2})$ nA, is achieved at a magnetic field gradient of 1.2 T/m. Since there is no further selection after the optical molasses section, there is no significant difference in flux in the cases with and without optical molasses.

The middle graph shows the transverse temperature plotted as a function of the magnetic field gradient. This temperature is the average between the separately measured temperature in the x and y directions. Without optical molasses, the lowest temperature is measured at $\nabla B = 0.6$ T/m and equals $(0.07^{+0.04}_{-0.03})$ mK. Furthermore, the trend indicates even lower temperatures at lower magnetic field gradients. The measured temperature is below the Doppler temperature of rubidium (0.143 mK), suggesting that sub-Doppler cooling effects do play a role, even in the presence of a magnetic field. Increasing the magnetic field gradient results in a higher temperature, stabilizing at $(0.2^{+0.1}_{-0.07})$ mK, which is near the Doppler temperature. Note that the lowest temperature and the highest flux are not achieved at the same magnetic field gradient. With the optical molasses enabled, the temperature does not change significantly in the measured range and is equal to $(0.04^{+0.02}_{-0.01})$ mK.

The bottom graph shows the equivalent brightness of the atomic beam. Without the additional optical molasses, the highest brightness reads $(1.0^{+0.8}_{-0.4}) \times 10^6$ A/(m^2 sr eV) at a magnetic field gradient of 1.2 T/m. Because of the lower temperature, the equivalent brightness is higher with the optical molasses enabled and reads $(5^{+5}_{-2}) \times 10^6$ A/(m^2 sr eV). As is argued at the end of Sec. II B, the atomic beam can be ionized and accelerated without major heating below currents of 10 pA. Therefore, the resulting ion source would be an improvement over the LMIS in terms of ion-beam brightness in this regime.

Table I summarizes the performance of the atomic beam. The flux, the temperature, the equivalent transverse reduced brightness, and the average longitudinal velocity are given at different positions in the setup. As can be seen, only

TABLE I. Summary of beam parameters at several points in the setup. All values are measured or calculated at a Knudsen source temperature of 413 K. The values measured after the 2D MOT and optical molasses are stated for the magnetic field gradient at which the equivalent reduced brightness is maximized.

Position	Φ (1/s)	T (mK)	B_r [A/(m^2 sr eV)]	$\langle v_z \rangle$ (m/s)
After collimated Knudsen source	$(9 \pm 4) \times 10^{13}$[a]	$(94 \pm 10) \times 10^{3}$[a]	(140 ± 40)[a]	321[b]
After 2D MOT	$(4^{+2}_{-1}) \times 10^{9}$	$(0.2^{+0.1}_{-0.07})$	$(1.0^{+0.8}_{-0.4}) \times 10^{6}$	(93 ± 2)
After optical molasses	$(3^{+2}_{-1}) \times 10^{9}$	$(0.04^{+0.02}_{-0.01})$	$(5^{+5}_{-2}) \times 10^{6}$	(93 ± 2)

[a]Value is adapted from previous measurements discussed in Ref. [27].
[b]Value is not measured but is calculated from Knudsen source temperature.

0.004% of the flux that is leaving the collimated Knudsen source is transmitted by the selection aperture. This low fraction is mostly caused by the fact that the atoms have a large spread in transverse velocity when leaving the collimation tube of the Knudsen source, as can be witnessed by the high transverse temperature at this point stated in Table I. Therefore, only a small fraction is being captured by the 2D MOT. However, by scanning the beam over the selection aperture by displacing the magnetic axis of the quadrupole, it is also found that the FWHM size of the beam is approximately 3× larger than the diameter of the selection aperture. This means that the total current of the beam is approximately 9× larger before the selection aperture, giving a second explanation for the large difference in flux before and after the 2D MOT. Note that the flux is of the same order as most of the atomic-beam sources discussed in the Introduction, which are aimed at producing a large flux of slow atoms. However, the difference between those sources is the higher flux density that is achieved here and, therefore, the higher brightness. The beam diameter of 100 μm (determined by the selection aperture) is roughly an order of magnitude smaller than that achieved in, for example, a 2D$^+$ MOT [16,17]. The two laser-cooling sections combined increase the equivalent transverse reduced brightness with a factor 4×10^4 to $(5^{+5}_{-2}) \times 10^6$ A(m^2 sr eV). This has not been achieved with a single trapping step when combined with an effusive source. However, a value of 2×10^7 A/(m^2 sr eV) has been achieved by compressing the beam from a 2D$^+$ MOT in a magneto-optical compressor [13] and a value of 3×10^7 A/(m^2 sr eV) has been realized using a setup incorporating a Zeeman slower [25].

E. Beam density vs source temperature

The last parameter that is varied is the temperature of the Knudsen source. Under the assumption of no collisions or other density-limiting effects, increasing the temperature of the source would lead to an increase in flux according to Eqs. (1) and (12) in Ref. [15]. However, it is known from experiments on 3D MOTs that, at high densities and intense resonant illumination, inelastic collisions between ground- and excited-state atoms [37] and attenuation and radiation-trapping effects [38] will limit the achievable density. Therefore, an experiment is performed in which the temperature of the Knudsen source is varied.

Figure 8 shows the beam density as a function of source temperature in two cases: with the magnetic field gradient set to the optimal value of 1.1 T/m and without any magnetic field. The figure also shows a scaling law that scales the first data point of both measurements with the flux coming from the Knudsen source [27]. Although the beam density does increase with increasing source temperature, Fig. 8 shows that the scaling law holds only for the lowest temperatures and in the case with no magnetic field gradient. At the highest temperature, the measurement and the scaling are off by a factor of 11 in the case without a magnetic gradient and a factor of 21 in the case with a magnetic gradient. This deviation from the scaling is attributed to three effects. First of all, in the determination of total flux of atoms effusing from the collimated Knudsen source (see Ref. [15]), it is observed that, at high temperatures, the flux is lower than would be expected from the model. At 433 K, the difference is a factor of 2, partly

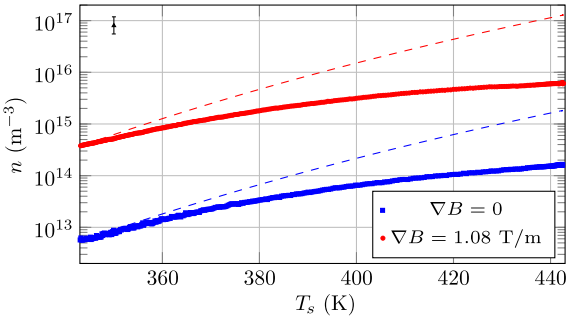

FIG. 8. Atomic-beam density after the 2D MOT as a function of the source temperature. The relative-uncertainty margin due to systematic errors is indicated with a black bar in the upper-left corner. Two measurements are shown: one in which the beam is only cooled ($\nabla B = 0$ T/m, the blue open circles) and one in which it is also compressed ($\nabla B = 1.1$ T/m, the red dots). In all measurements, the detuning of the cooling laser is set to -1.1Γ and the detuning of the probe laser is set to 0 MHz. As a reference, the dashed lines show a scaling of the first data point, with the theoretical flux coming from the Knudsen source under the assumption of no collisions inside the collimation tube [27].

explaining the difference in this experiment. In the measurement of the flux from the collimated Knudsen source, it is also observed that the transverse velocity distribution of the atoms is broadened due to collisions in the collimation tube. This broadening reduces the centerline intensity and thus reduces the fraction of atoms that can be captured by the 2D MOT. Between 343 and 433 K, the width of the velocity distribution increases by a factor of 2, suggesting that the capturable fraction decreases by a factor of 4. The effects of a lower flux and a broader transverse velocity distribution from the collimated Knudsen source can explain most of the difference between the results from the measurement without a magnetic gradient and the scaling law. The additional limiting of density in the experiment in which the magnetic field is enabled can not be explained by effects caused by the collimated Knudsen source. However, as can be seen from the results, at high temperatures, the beam density approaches 10^{16} m^{-3}, which is the density in which collisions between excited- and ground-state atoms and radiation-trapping effects start to play a role in MOTs [37–39]. More-advanced laser-cooling schemes using a repumper laser beam that has a dark spot in the very center of the atomic beam may allow us to overcome this limitation [39]. Because of the added complexity, such schemes are not pursued in this experiment.

Ultimately, a beam density of $(6^{+3}_{-2}) \times 10^{15}$ m^{-3} is reached. This beam density translates to a beam-flux equivalent of $(0.6^{+0.3}_{-0.2})$ nA through the selection aperture and an equivalent brightness of $(6^{+5}_{-2}) \times 10^6$ $A/(m^2\,sr\,eV)$. The current Knudsen source does not allow for higher temperatures than approximately 443 K. However, linear extrapolation of the measurement teaches that only a 20% increase in density, and thus brightness, can be achieved when the source temperature is raised by 20 K. Since part of the deviation from the scaling law is caused by collisions inside the collimation tube of the Knudsen source, a slightly higher flux can be expected when using a Knudsen source collimated by an aperture instead of a tube or the more-complex candlestick oven design [40]. However, ultimately the density will be limited by the previously mentioned effects.

With the maximum beam density measured and the cross section for absorption on resonance [32], the optical density of the beam can be calculated to be 9×10^{-2} at the position of the selection aperture. This means that if the LIF experiment is performed at the aperture, 91% of the emitted photons would be transmitted through the atomic beam. The resulting correction for (re)absorption is smaller than the error margins.

IV. CONCLUSION

In this paper, the properties of an atomic rubidium beam resulting from 2D magneto-optical trapping of effusive atoms from a collimated Knudsen source are evaluated. Laser-induced fluorescence is used to image the beam and determine its flux and transverse temperature. As knowledge of the longitudinal velocity of the atoms is required for both of these parameters, the longitudinal velocity distribution is measured as well. The average longitudinal velocity is found to be dependent on the magnetic field gradient in the 2D MOT and has a value of 50–100 m/s. As the beam is intended to be photoionized and applied as a source for a focused ion beam, its flux is expressed in units of current and the equivalent reduced brightness is also calculated. In a single 2D magneto-optical trapping step, the maximum equivalent beam current found is $(0.6^{+0.3}_{-0.2})$ nA and the transverse temperature is $(0.2^{+0.1}_{-0.07})$ mK. Together, these values combine into an equivalent transverse reduced brightness of $(1^{+0.8}_{-0.4}) \times 10^6$ $A/(m^2\,sr\,eV)$. With an additional optical-molasses step, this value is increased to $(6^{+5}_{-2}) \times 10^6$ $A/(m^2\,sr\,eV)$ by lowering the transverse temperature of the beam. When ionized, this would be a 6× improvement over the brightness of the liquid-metal ion source, 300× larger than any MOT-based ion source [10,41] and similar to the estimated brightness from the $2D^+$ MOT–based source by Knuffman *et al.* [13].

In future research, photoionization of the atomic beam will be investigated. To reach an ionization degree of 80%, an ionization laser intensity of 2×10^{10} W/m^2 is needed. In order to reach this intensity over a large cross-section area of the beam, a buildup cavity will be used to enhance the power of a commercially available laser system. Furthermore, previous work [28] predicted that, by immediately accelerating the ions in a sufficiently large but realistic electric field, the transverse reduced brightness of the beam could be conserved at currents below 10 pA. Therefore, nanometer-sized waists are expected when focusing a 30-keV beam containing 1 pA.

ACKNOWLEDGMENTS

This research was supported by the Dutch Technology Foundation STW Grant No. 12199, which is part of the Netherlands Organisation for Scientific Research (NWO), and which is partly funded by the Ministry of Economic Affairs. The research was also supported by FEI Company, Pulsar Physics and Coherent Inc. We would like to thank Bas van der Geer and Eddy Rietman for their design work on the magnetic quadrupole, and Eddy Rietman, Harry van Doorn, and Iman Koole for their technical support.

G. t. H. and S. H. W. W. contributed equally to this work.

APPENDIX: UNCERTAINTY ANALYSIS

In linear uncertainty analysis, the dependence of the end results on its parameters is linearized. This linearization gives incorrect results if the relative errors, $\Delta i/i$, are large. Therefore, the upper and lower (systematic) values for the flux, the temperature, and the brightness are calculated differently by filling in the parameters plus or minus their

TABLE II. Typical experimental parameters and their systematic uncertainties.

Parameters (unit)	Symbol	Value ± error
Probe laser detuning (MHz)	δ_p	0 ± 1
Probe laser-beam intensity (W/m^2)	I	96 ± 10
Probe laser-beam angle for v_z measurement (deg)	θ	14.8 ± 0.5
Saturation parameter for linear polarized light (W/m^2)	I_{sat}	$31.8 + 7.2 - 0.0$
Drift distance (m)	Δz	0.20 ± 0.02
Camera shutter time (s)	t_c	1.000 ± 0.001
Camera gain (counts/photon)	G	2.08 ± 0.08
Camera pixel size (μm)	l_{px}	5.86
Longitudinal image size (mm)	l_{img}	1.172
Probe window transmission (%)	T_w	90 ± 2
Filter transmission (%)	T_f	89 ± 1
Selection aperture radius (μm)	R	50 ± 1
Lens object distance (m)	o	0.237 ± 0.005
Lens image distance (m)	b	0.105 ± 0.005
Lens aperture radius (mm)	r_l	6 ± 0.5
Resulting inverse-averaged longitudinal velocity (m/s)	$\overline{v_z}$	82 ± 3
Resulting inverse-squared averaged longitudinal velocity (m/s)	$\tilde{v_z}$	79 ± 3

uncertainty margin in such a way that the maximal or minimal value for the flux, the temperature, or the brightness is found. The complete equation used for finding the transverse temperature from the experiment is given by

$$T_x = \frac{m}{k_B}\frac{\tilde{v_z}^2}{(\Delta z)^2}\left(\frac{o^2 l_{\mathrm{px}}^2}{b^2}\sigma_{\mathrm{px}}^2 - (R/2)^2\right), \tag{A1}$$

in which σ_{px} is the root-mean-square width of the fitted normal distribution in units of camera pixels and l_{px} is the width of a single pixel. The complete equation for the flux is found by combining Eqs. (3)–(5), resulting in

$$\Phi = \frac{4}{\Gamma}\frac{b\overline{v_z}oC}{l_{\mathrm{img}}\rho_{ee}(\delta_p)r_l^2 t_c T_w T_f G}, \tag{A2}$$

into which l is substituted, with $l = l_{\mathrm{img}}(o/b)$, in which l_{img} is the longitudinal size of the image. Using the same substitution and Eq. (6) for the density results in

$$n = \frac{4}{\pi\Gamma}\frac{boC}{R^2 l_{\mathrm{img}}\rho_{ee}(\delta_p)r_l^2 t_c T_w T_f G}. \tag{A3}$$

The complete equation for the equivalent brightness can be found by combining Eqs. (7), (A1), and (A2), resulting in

$$B_r = \frac{4e}{m\pi^2\Gamma}\frac{b^3 o(\Delta z)^2}{R^2 l_{\mathrm{img}}\rho_{ee}(\delta_p)r_l^2 t_c T_w T_f G} \times \frac{C\bar{v}_z}{\tilde{v_z}^2[o^2 l_{\mathrm{px}}^2\sigma_{\mathrm{px}}^2 - b^2(R/2)^2]}. \tag{A4}$$

Typical values for all of the parameters used are given in Table II together with the uncertainties in them. With these values, the relative uncertainties are +62% and −37% for the temperature, +51% and −32% for the flux, +48% and −31% for the density, and +80% and −30% for the equivalent brightness.

[1] J. Weiner, V. S. Bagnato, S. Zilio, and P. S. Julienne, Experiments and theory in cold and ultracold collisions, Rev. Mod. Phys. **71**, 1 (1999).

[2] A. D. Cronin, J. Schmiedmayer, and D. E. Pritchard, Optics and interferometry with atoms and molecules, Rev. Mod. Phys. **81**, 1051 (2009).

[3] J. J. McClelland, A. V. Steele, B. Knuffman, K. A. Twedt, A. Schwarzkopf, and T. M. Wilson, Bright focused ion beam sources based on laser-cooled atoms, Appl. Phys. Rev. **3**, 011302 (2016).

[4] J. Orloff, High-resolution focused ion beams, Rev. Sci. Instrum. **64**, 1105 (1993).

[5] V. Raffa, P. Castrataro, A. Menciassi, and P. Dario, in *Applied Scanning Probe Methods II: Scanning Probe Microscopy Techniques*, edited by B. Bhushan and H. Fuchs (Springer, Berlin, Heidelberg, 2006).

[6] J Gierak, Focused ion beam technology and ultimate applications, Semicond. Sci. Technol. **24**, 043001 (2009).

[7] C. W. Hagen, E. Fokkema, and P. Kruit, Brightness measurements of a gallium liquid metal ion source, J. Vac. Sci. Technol. B **26**, 2091 (2008).

[8] A. E. Bell, K. Rao, G. A. Schwind, and L. W. Swanson, A low-current liquid metal ion source, J. Vac. Sci. Technol. B **6**, 927 (1988).

[9] J. Orloff, Fundamental limits to imaging resolution for focused ion beams, J. Vac. Sci. Technol. B **14**, 3759 (1996).

[10] J. L. Hanssen, S. B. Hill, J. Orloff, and J. J. McClelland, Magneto-optical-trap-based, high brightness ion source for use as a nanoscale probe, Nano Lett. **8**, 2844 (2008).
[11] M. P. Reijnders, P. A. van Kruisbergen, G. Taban, S. B. van der Geer, P. H. A. Mutsaers, E. J. D. Vredenbregt, and O. J. Luiten, Low-Energy-Spread Ion Bunches from a Trapped Atomic Gas, Phys. Rev. Lett. **102**, 034802 (2009).
[12] B. G. Freinkman, A. V. Eletskii, and S. I. Zaitsev, A proposed laser source of ions for nanotechnology, Microelectron. Eng. **73–74**, 139 (2004).
[13] B. Knuffman, A. V. Steele, and J. J. McClelland, Cold atomic beam ion source for focused ion beam applications, J. Appl. Phys. **114**, 044303 (2013).
[14] L. Kime, A. Fioretti, Y. Bruneau, N. Porfido, F. Fuso, M. Viteau, G. Khalili, N. Santic, A. Gloter, B. Rasser, P. Sudraud, P. Pillet, and D. Comparat, High-flux monochromatic ion and electron beams based on laser-cooled atoms, Phys. Rev. A **88**, 033424 (2013).
[15] S. H. W. Wouters, G. ten Haaf, R. P. M. J. W. Notermans, N. Debernardi, P. H. A. Mutsaers, O. J. Luiten, and E. J. D. Vredenbregt, Performance predictions for a laser-intensified thermal beam for use in high-resolution focused-ion-beam instruments, Phys. Rev. A **90**, 063817 (2014).
[16] K. Dieckmann, R. J. C. Spreeuw, M. Weidemüller, and J. T. M. Walraven, Two-dimensional magneto-optical trap as a source of slow atoms, Phys. Rev. A **58**, 3891 (1998).
[17] S. Chaudhuri, S. Roy, and C. S. Unnikrishnan, Realization of an intense cold Rb atomic beam based on a two-dimensional magneto-optical trap: Experiments and comparison with simulations, Phys. Rev. A **74**, 023406 (2006).
[18] W. Xiao-long, C. Bing, and W. Bin, Intense source of cold cesium atoms based on a two-dimensional magneto-optical trap with independent axial cooling and pushing, Chin. Phys. B **25**, 063701 (2016).
[19] J. Schoser, A. Batar, R. Low, V. Schweikhard, A. Grabowski, Yu. B. Ovchinnikov, and T. Pfau, Intense source of cold Rb atoms from a pure two-dimensional magneto-optical trap, Phys. Rev. A **66**, 023410 (2002).
[20] J. J. Arlt, O. Marago, S. Webster, S. Hopkins, and C. J. Foot, A pyramidal magneto-optical trap as a source of slow atoms, Opt. Commun. **157**, 303 (1998).
[21] A. Camposeo, A. Piombini, F. Cervelli, F. Tantussi, F. Fuso, and E. Arimondo, A cold cesium atomic beam produced out of a pyramidal funnel, Opt. Commun. **200**, 231 (2001).
[22] T. G. Tiecke, S. D. Gensemer, A. Ludewig, and J. T. M. Walraven, High-flux two-dimensional magneto-optical-trap source for cold lithium atoms, Phys. Rev. A **80**, 013409 (2009).
[23] G. Lamporesi, S. Donadello, S. Serafini, and G. Ferrari, Compact high-flux source of cold sodium atoms, Rev. Sci. Instrum. **84**, 063102 (2013).
[24] F. Lison, P. Schuh, D. Haubrich, and D. Meschede, High-brilliance Zeeman-slowed cesium atomic beam, Phys. Rev. A **61**, 013405 (1999).
[25] W. DeGraffenreid, J. Ramirez-Serrano, Y.-M. Liu, and J. Weiner, Continuous, dense, highly collimated sodium beam, Rev. Sci. Instrum. **71**, 3668 (2000).
[26] C.-C. Tsao, Y. Wang, J. Weiner, and V. S. Bagnato, Optical collimation and compression of a thermal atomic beam, J. Appl. Phys. **80**, 8 (1996).
[27] S. H. W. Wouters, G. ten Haaf, P. H. A. Mutsaers, and E. J. D. Vredenbregt, Design and experimental validation of a compact collimated Knudsen source, Rev. Sci. Instrum. **87**, 083305 (2016).
[28] G. ten Haaf, S. H. W. Wouters, S. B. van der Geer, E. J. D. Vredenbregt, and P. H. A. Mutsaers, Performance predictions of a focused ion beam from a laser cooled and compressed atomic beam, J. Appl. Phys. **116**, 244301 (2014).
[29] M. Viteau, M. Reveillard, L. Kime, B. Rasser, P. Sudraud, Y. Bruneau, G. Khalili, P. Pillet, D. Comparat, I. Guerri, A. Fioretti, D. Ciampini, M. Allegrini, and F. Fuso, Ion microscopy based on laser-cooled cesium atoms, Ultramicroscopy **164**, 70 (2016).
[30] J. Nellessen, J. Werner, and W. Ertmer, Magneto-optical compression of a monoenergetic sodium atomic beam, Opt. Commun. **78**, 300 (1990).
[31] P. Oxley and J. Wihbey, Precision atomic beam density characterization by diode laser absorption spectroscopy, Rev. Sci. Instrum. **87**, 093103 (2016).
[32] D. A. Steck, Rubidium 85D Line Data, revision 2.1.6, http://steck.us/alkalidata (September 20, 2013).
[33] G. C. Bjorklund, M. D. Levenson, W. Lenth, and C. Ortiz, Frequency modulation (FM) spectroscopy, Appl. Phys. B **32**, 145 (1983).
[34] C. J. Foot, *Atomic Physics* (Oxford University Press, New York, 2005).
[35] O. J. Luiten, B. J. Claessens, S. B. Van Der Geer, M. P. Reijnders, G. Taban, and E. J. D. Vredenbregt, Ultracold electron sources, Int. J. Mod. Phys. A **22**, 3882 (2007).
[36] R. Chang, A. L. Hoendervanger, Q. Bouton, Y. Fang, T. Klafka, K. Audo, A. Aspect, C. I. Westbrook, and D. Clement, Three-dimensional laser cooling at the Doppler limit, Phys. Rev. A **90**, 063407 (2014).
[37] C. D. Wallace, T. P. Dinneen, K.-Y. N. Tan, T. T. Grove, and P. L. Gould, Isotopic Difference in Trap Loss Collisions of Laser Cooled Rubidium Atoms, Phys. Rev. Lett. **69**, 897 (1992).
[38] T. Walker, D. Sesko, and C. Wieman, Collective Behavior of Optically Trapped Neutral Atoms, Phys. Rev. Lett. **64**, 408 (1990).
[39] W. Ketterle, K. B. Davis, Michael A. Joffe, A. Martin, and D. E. Pritchard, High Densities of Cold Atoms in a Dark Spontaneous-Force Optical Trap, Phys. Rev. Lett. **70**, 2253 (1993).
[40] M. R. Walkiewicz, P. J. Fox, and R. E. Scholten, Candlestick rubidium beam source, Rev. Sci. Instrum. **71**, 3342 (2000).
[41] N. Debernardi, R. W. L. van Vliembergen, W. J. Engelen, K. H. M. Hermans, M. P. Reijnders, S. B. van der Geer, P. H. A. Mutsaers, O. J. Luiten, and E. J. D. Vredenbregt, Optimization of the current extracted from an ultracold ion source, New J. Phys. **14**, 083011 (2012).